AGU PUBLICATIONS

Geophysical Research Letters

RESEARCH LETTER
10.1002/2016GL069191

Special Section:
First results from NASA's Magnetospheric Multiscale (MMS) Mission

Key Points:
- We detect electron scale current sheet
- We observe electron jets
- We observe particle heating and energy dissipation

Correspondence to:
E. Yordanova,
eya@irfu.se

Citation:
Yordanova, E., et al. (2016), Electron scale structures and magnetic reconnection signatures in the turbulent magnetosheath, *Geophys. Res. Lett.*, *43*, 5969–5978, doi:10.1002/2016GL069191.

Received 15 APR 2016
Accepted 19 MAY 2016
Accepted article online 27 MAY 2016
Published online 20 JUN 2016

©2016. American Geophysical Union. All Rights Reserved.

Electron scale structures and magnetic reconnection signatures in the turbulent magnetosheath

E. Yordanova[1], Z. Vörös[2,3,4], A. Varsani[2], D. B. Graham[1], C. Norgren[1], Yu. V. Khotyaintsev[1], A. Vaivads[1], E. Eriksson[1], R. Nakamura[2], P.-A. Lindqvist[5], G. Marklund[5], R. E. Ergun[6], W. Magnes[2], W. Baumjohann[2], D. Fischer[2], F. Plaschke[2], Y. Narita[2], C. T. Russell[7], R. J. Strangeway[7], O. Le Contel[8], C. Pollock[9], R. B. Torbert[10], B. J. Giles[9], J. L. Burch[10], L. A. Avanov[9], J. C. Dorelli[9], D. J. Gershman[9,11], W. R. Paterson[9], B. Lavraud[12,13], and Y. Saito[14]

[1]Swedish Institute of Space Physics, Uppsala, Sweden, [2]Space Research Institute, Austrian Academy of Sciences, Graz, Austria, [3]Department of Geophysics and Space Sciences, Eötvös Loránd University, Budapest, Hungary, [4]Geodetic and Geophysical Institute, RCAES, Hungarian Academy of Sciences, Sopron, Hungary, [5]Space and Plasma Group, Royal Institute of Technology, Stockholm, Sweden, [6]Laboratory of Atmospheric and Space Physics, University of Colorado Boulder, Boulder, Colorado, USA, [7]Institute of Geophysics and Planetary Physics, University of California, Los Angeles, USA, [8]Laboratoire de Physique des Plasmas, CNRS/Ecole Polytechnique/UPMC/Univ. Paris Sud/Obs. de Paris, Paris, France, [9]NASA Goddard Space Flight Center, Greenbelt, Maryland, USA, [10]Southwest Research Institute, San Antonio, Texas, USA, [11]Astronomy Department, University of Maryland, College Park, Maryland, USA, [12]IRAP, CNRS, Toulouse, France, [13]CNRS, Toulouse, France, [14]JAXA, Tokyo, Japan

Abstract Collisionless space plasma turbulence can generate reconnecting thin current sheets as suggested by recent results of numerical magnetohydrodynamic simulations. The Magnetospheric Multiscale (MMS) mission provides the first serious opportunity to verify whether small ion-electron-scale reconnection, generated by turbulence, resembles the reconnection events frequently observed in the magnetotail or at the magnetopause. Here we investigate field and particle observations obtained by the MMS fleet in the turbulent terrestrial magnetosheath behind quasi-parallel bow shock geometry. We observe multiple small-scale current sheets during the event and present a detailed look of one of the detected structures. The emergence of thin current sheets can lead to electron scale structures. Within these structures, we see signatures of ion demagnetization, electron jets, electron heating, and agyrotropy suggesting that MMS spacecraft observe reconnection at these scales.

1. Introduction

The main goal of Magnetospheric Multiscale (MMS) mission is the multipoint study of microphysics of magnetic reconnection (MR) targeting the structures within the electron diffusion region [*Burch et al.*, 2015, 2016]. Additional science goals include the understanding of the physics of particle acceleration and the clarification of the role of plasma turbulence in fast collisionless MR. On the other hand, high Reynolds number magnetohydrodynamic and Particle-in-Cell (PIC) simulations show that turbulence can also generate spatially intermittent, thin, and reconnecting current sheets [*Greco et al.*, 2008; *Servidio et al.*, 2009; *Wan et al.*, 2015]. The occurrence of MR in the turbulent terrestrial magnetosheath was also confirmed by Cluster measurements [*Retinò et al.*, 2007]. In turbulent space plasmas the ion-electron-scale current sheets are found to be associated with locally enhanced heating and energy dissipation [*Osman et al.*, 2012, 2014; *Chasapis et al.*, 2015]. Although in collisionless plasmas only approximate measures of energy dissipation can be introduced [*Matthaeus et al.*, 2015], the generation of spatially intermittent current sheets indicates that the associated kinetic dissipation, in which MR can play a crucial role, is spatially inhomogeneous. Despite the highly localized dissipation, the heating of the plasma can be significant [*Servidio et al.*, 2012]. A recent experimental study based on Cluster data shows that turbulence-generated thin proton-scale current sheets are ubiquitous in the magnetosheath downstream of a quasi-parallel bow shock [*Vörös et al.*, 2016]. This implies that turbulence may also generate numerous reconnecting current sheets which can be studied through high-resolution field, plasma, and particle measurements available from MMS. Secondary MR sites can also occur at MR generated flux ropes or in turbulent reconnection exhausts [*Lapenta et al.*, 2015]. The large number of turbulence-generated or secondary MR sites may substantially increase the probability of MMS encounter by the electron diffusion region.

Global hybrid and fully kinetic simulations of the Earth's magnetosphere indicate that flux ropes and other plasma structures in the turbulent magnetosheath can also be generated by the interaction of the solar wind with the bow shock [*Karimabadi et al.*, 2014].

In this paper we investigate a possible MR site in the turbulent terrestrial magnetosheath by detailed analysis of field, plasma, and particle observation by MMS spacecraft. The different terms in the generalized Ohm's law are calculated and their relative contribution characterizing the ion and electron motion. Additionally, dimensionless proxies characterizing electron demagnetization and frozen flux violation are calculated from single point measurements [*Zenitani et al.*, 2011; *Aunai et al.*, 2013; *Scudder et al.*, 2015].

2. Data and Instrumentation

The merged digital fluxgate (FGM) [*Russell et al.*, 2014] and search coil (SCM) [*Le Contel et al.*, 2014] data were developed by using instrument frequency and timing models that were created during the FIELDS integration test campaign [*Torbert et al.*, 2014]. These models are based on linear filter functions and can correct the respective frequency responses of the instruments in gain and phase. Using these models in-flight data was corrected and data were added using low- and high-pass filter functions. Thus, the data set analyzed here consists of data below 4 Hz originating from FGM, data above—from SCM and in the crossover region both data sets were used [*Fischer et al.*, 2016]. The electric field data from Electric Double Probes (EDP) instrument are available with time resolution of 8 kHz [*Torbert et al.*, 2014; *Ergun et al.*, 2016; *Lindqvist et al.*, 2016]. Ion and electron moments from Fast Plasma Investigation (FPI) instrument [*Pollock et al.*, 2016] have time resolution 150 ms and 30 ms, respectively.

3. Event Overview

On 30 November 2015 between 00:21 and 00:26 UT the MMS spacecraft were situated in the compressed turbulent magnetosheath, downstream of a quasi-parallel bow shock. At the same time, the solar wind monitors (OMNI database) observed an extended high-density compressional region at the leading edge of a high-speed stream, associated with a significant geomagnetic response (not shown). The overview plot (Figure 1) shows the observed field and plasma parameters between 00:26:03 and 00:26:18 UT. It is demonstrated here that this 15 s long interval contains a flux rope and its interacting boundary/region comprising discontinuities, narrow current structures, and magnetic reconnection. These are the typical structures seen in simulations of plasma turbulence [*Greco et al.*, 2008; *Servidio et al.*, 2009; *Wan et al.*, 2015]. Figures 1a–1d show the total magnetic field B_{t_k} and magnetic components B_{x_k}, B_{y_k}, and B_{z_k} in spacecraft reference frame. Indices k refer to MMS spacecraft. The so-called partial variance of increments (PVIs), often used in studies of plasma turbulence to detect discontinuities and/or current sheets, has been here adapted to multispacecraft measurements [*Chasapis et al.*, 2015]. The signal PVI_{ij} has been calculated between spacecraft pairs i, j ($i, j = 1$–4 are the number of MMS spacecraft). PVI_{ij} is depicted in the Figure 1e and is defined through

$$\mathrm{PVI}_{ij}(t) = \sqrt{\frac{|\,\Delta\mathbf{B}_{ij}(t)\,|^2}{\left\langle |\,\Delta\mathbf{B}_{ij}\,|^2 \right\rangle}}. \tag{1}$$

The latitude θ_2 and longitude ϕ_2 of magnetic field vector orientation for MMS 2 are shown in Figure 1f. Figure 1g contains the pressures (total, dynamic, magnetic, ion thermal, and electron thermal). Here the different pressure terms are shown with the same color for each spacecraft. The magnitudes of ion and electron speeds, $\mathbf{V}\mathrm{i}_k$ and $\mathbf{V}\mathrm{e}_k$, are shown in Figures 1h and 1i, respectively. The magnitudes of electric field $\mathbf{E}_k$ in spacecraft reference frame and the magnitudes of current densities $\mathbf{J}_k$ are shown in Figures 1j and 1k, respectively. $\mathbf{J}_k$'s are calculated for each spacecraft from plasma measurements through $\mathbf{J}_k = Nq(\mathbf{V}\mathrm{i}_k - \mathbf{V}\mathrm{e}_k)$, where N is the plasma density and q is the charge of particles. The thick magenta line in Figure 1k corresponds to the magnitude of the current density $\mathbf{J}_{\mathrm{curl}}$, estimated in the tetrahedron barycenter by using the curlometer technique [*Dunlop et al.*, 2002]. The cyan curve, noted as $\mathbf{J}_{\mathrm{plasma}}$ in the same subplot, is the average plasma current over the four spacecraft. Its comparison with the current obtained from the curlometer demonstrates the very good agreement in the current estimation by the two approaches.

There exist two different physical regions which can be identified in Figure 1. A twisted flux rope extends roughly from 00:26:10 UT to the end of the time interval. It can be identified on the basis of the slow rotation

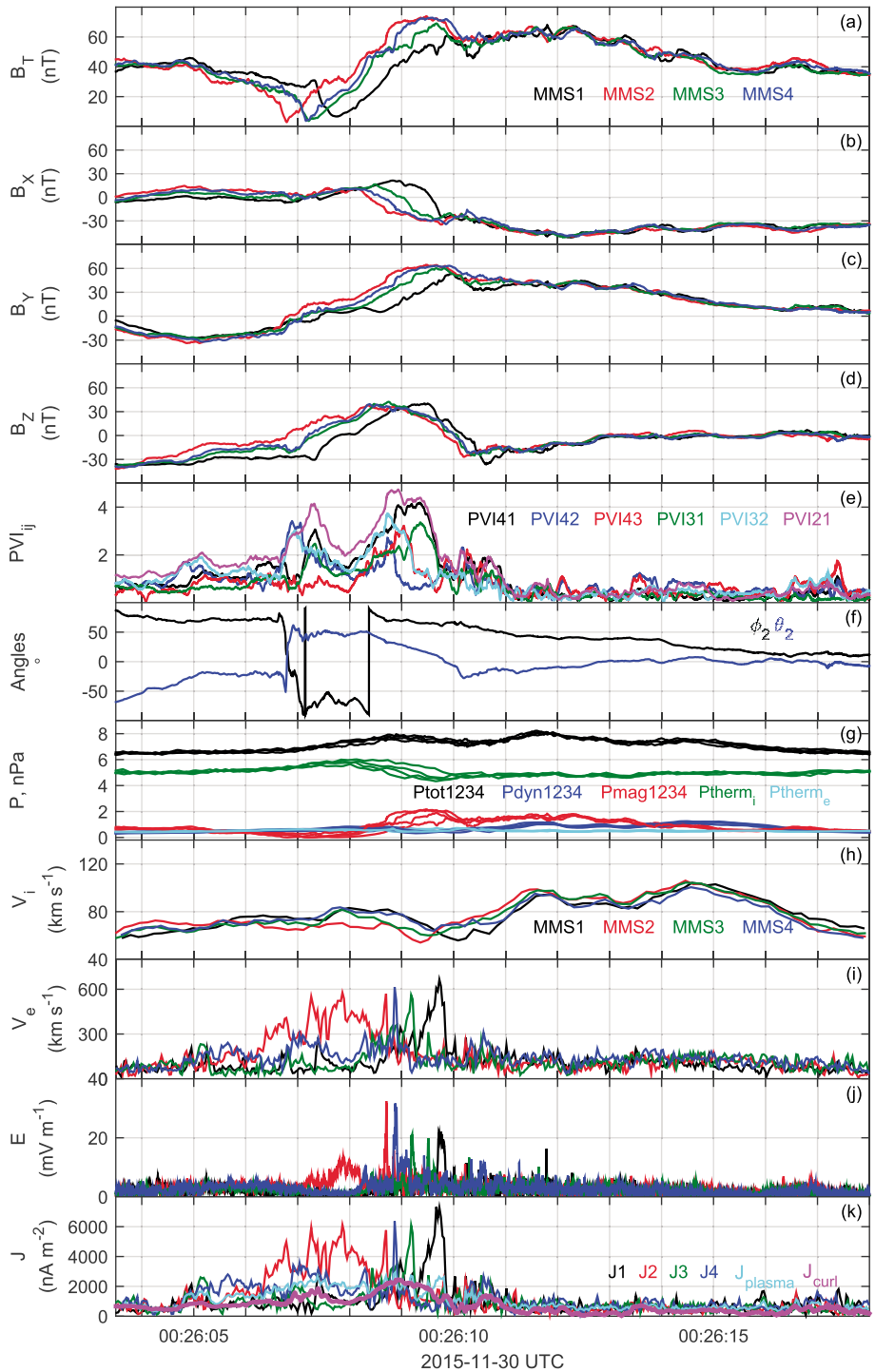

Figure 1. Field and plasma parameters in spacecraft coordinates: (a) Magnetic field magnitude for the four MMS spacecraft (color coded); (b–d) magnetic field components; (e) PVI_{ij} from pairs of spacecraft (i,j = MMS 1–4); (f) the elevation and azimuthal angle of the magnetic field for MMS 2; (g) pressure for all spacecraft: total (black), dynamical (blue), magnetic (red), ion thermal (green), and electron thermal (cyan); (h) ion velocity for all spacecraft; (i) electron velocity; (j) electric field magnitude; and (k) electric current from plasma for each spacecraft, the averaged over all spacecraft plasma current (cyan) and the current from curlometer (magenta).

and sign change of the magnetic field, seen in Bz_k (Figure 1d), changing from −32 nT (minimum) to +8 nT (maximum). The slow rotation is also seen in θ_2. Other signatures of the flux rope include the maxima of Bt_k (Figure 1a) and total pressure P_{tot} (Figure 1g) between 00:26:11 and 00:26:13 UT. Although the ion P_{therm} is higher then P_{mag}, the profile of P_{tot} having maximum near the rope axis [*Zaqarashvili et al.*, 2014] is determined by P_{mag}. To support the flux rope identification, we have calculated the dot product between $\mathbf{J}_{curl}$ and **B**. If a helical flux rope is carrying a current, this current should be roughly along B, therefore, $\mathbf{J}_{curl} \cdot \mathbf{B} \neq 0$, as it has been verified for our case (not shown).

At the left border of the flux rope (roughly between 00:26:05 and 00:26:10 UT) we observe a distinct feature in all parameters. Further in the paper we will refer to it as the region of interest. Within this region the differences between magnetic field values (Figures 1a–1d) become larger, indicating increased magnetic gradients. PVI_{ij} shows the occurrence of two discontinuities (Figure 1e), where also the orientations of magnetic vectors (θ and ϕ in subplot 1f) exhibit sudden changes. At the same time, there exist significant changes and narrow peaks in Ve_k, E_k, and J_k, while the Vi_k variations are much smaller, indicating the occurrence of differential motion between ions and electrons at narrow structures. The electron inertial length in this region is ~0.7 km and the Doppler shifted frequency associated with this scale corresponds to about 26 Hz. These structures are narrower than the interspacecraft separation (~10 km); therefore, the curlometer cannot detect them (the magenta curve of J_{curl} is much smoother in subplot 1k). The narrow peaks in $\mathbf{V}e_k$, $\mathbf{E}_k$, and $\mathbf{J}_k$ between 00:26:08.5 and 00:26:10 UT are subsequently seen by all spacecraft, therefore representing real spatial structures.

4. The Event in a New Coordinate System

To better understand the event presented in Figure 1 the physical variables were rotated to the field-aligned coordinate system, in which X: **B**, Y: **E**×**B**, and Z: **B**×**E**×**B**. We have chosen a rotation matrix at the instant of electron speed maximum before 00:26:10 UT in Figure 2 (Figure 2d), which served as a global coordinate system for the whole event. In this coordinate system the largest variations of the magnetic field occur at the border of the flux rope in B_x and B_z components, while B_y is changing slowly (Figures 2a–2c). The flux rope interval after 00:26:10 UT is characterized by a slow rotation of the magnetic field. The electron speed components (Figures 2d–2f) show occurrence of jets at the border, while the ion speed increase is smaller and the variation is smoother (Figures 2g–2i). Similar electron jets have been observed at the magnetopause [*Khotyaintsev et al.*, 2016, this issue]. The ion and electron Alfvén speeds vary between spacecraft from 115 to 125 km/s . Electron and proton parallel and perpendicular temperatures are shown in Figures 2j and 2k. $Te_{\parallel}$ (Figure 2j) shows two peaks associated with temperature anisotropy and parallel electron heating at the left and right borders of the region between 00:26:05 and 00:26:11 UT in all spacecraft. Similar increases have been observed by recent MMS measurements at the magnetopause near the diffusion region and have been interpreted as evidence for a potential reconnection exhaust [*Graham et al.*, 2016; *Lavraud et al.*, 2016]. The ion temperature anisotropy, however, is absent within this region (Figure 2k). The slight increase of ion plasma density (Figure 2l) together with the increase of magnetic field (Figure 2a) and total/magnetic pressure (Figure 1g) between 00:26:09 and 00:26:11 UT indicates that this is a compressional region. The fluctuations and temperature anisotropies after 00:26:11 UT are associated with the flux rope again.

5. Generalized Ohm's Law Terms

In collisionless plasmas magnetic reconnection represents a multiscale process where characteristic reconnection structures over different scales can be observed. It is described by the generalized Ohm's law been written in terms of the electric field **E** [*Khotyaintsev et al.*, 2006]:

$$\mathbf{E} + \mathbf{V_i} \times \mathbf{B} = \frac{\mathbf{J} \times \mathbf{B}}{ne} - \frac{\nabla \cdot \mathbf{P}_e}{ne}, \tag{2}$$

where the electron inertia terms are neglected, **V** is the plasma bulk flow speed, **J** is the current density, $\mathbf{P}_e$ is the electron pressure tensor, **E** is the electric field in spacecraft frame, **B** is the magnetic field, m_e is the electron mass, n is the number density, and e is the proton charge. All quantities have been transformed in the new coordinate system described in the previous section. The z (out of plane) components of the terms in the

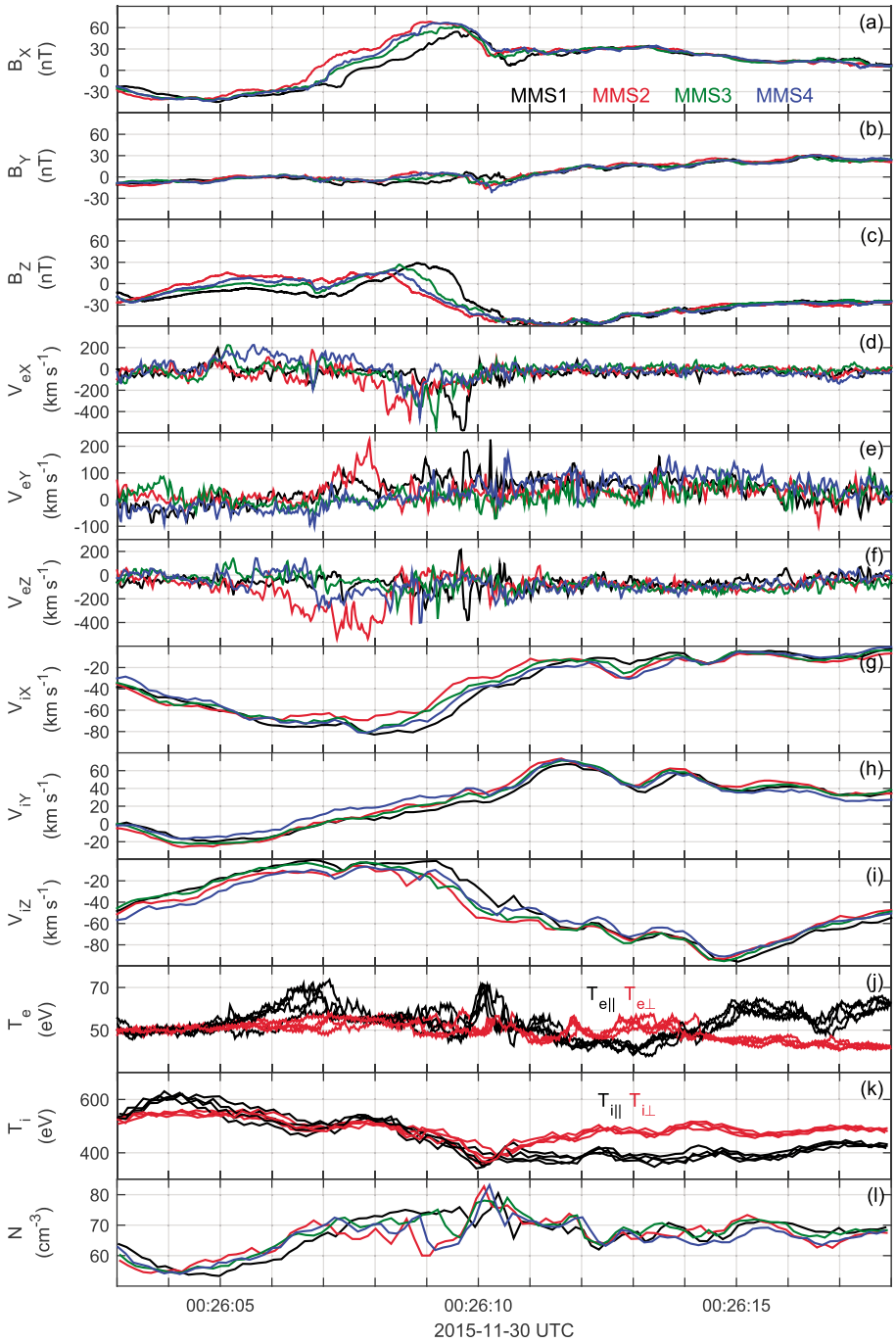

Figure 2. Field and plasma parameters in the rotated coordinate system: (a–c) magnetic field components for all spacecraft; (d–f) electron speed components; (g–i) ion speed components; (j and k) parallel (black) and perpendicular (red) to the background magnetic field electron and ion temperature for all spacecraft, respectively; and (l) ion density.

generalized Ohm's law and their relative strength indicate if the spacecraft are crossing the ion or electron diffusion regions [*Nakamura et al.*, 2016]. The different terms in the Ohm's law are plotted in Figures 3a–3e. The $(\mathbf{V}_i \times \mathbf{B})_z$ is small (Figure 3a); however, the electric field in the electron frame $(\mathbf{E} + \mathbf{V}_e \times \mathbf{B})_z$ is large around 00:26:10 UT (Figure 3b). The Hall term $(\mathbf{J} \times \mathbf{B}/\mathrm{ne})_z$ in Figure 3c indicates that $(\mathbf{V}_e \times \mathbf{B})_z \gg (\mathbf{V}_i \times \mathbf{B})_z$ and the differential motion of electrons and ions leads to significant Hall terms. The $\mathbf{E} \cdot \mathbf{J}$ reaching large values in the region of interest (Figure 3d) indicates that electromagnetic energy is converted to thermal and kinetic energies.

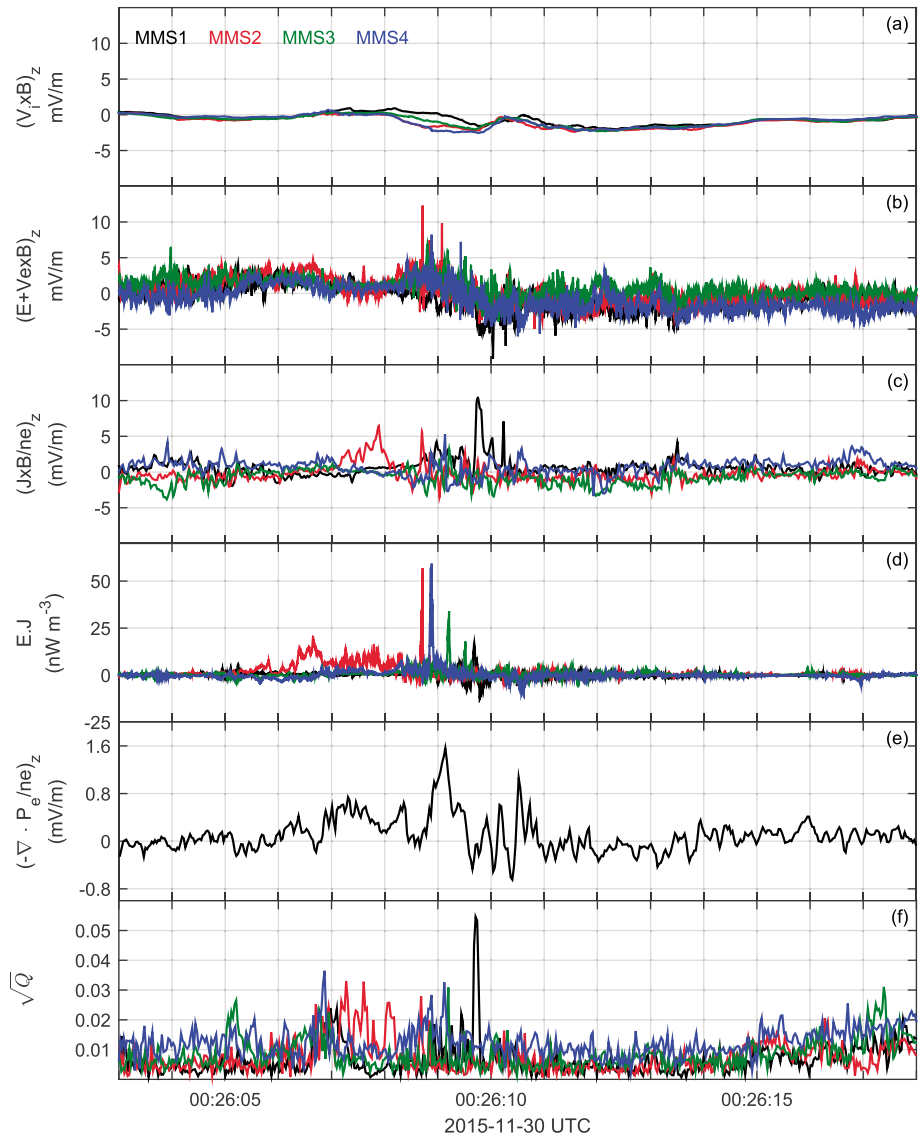

Figure 3. Generalized Ohm's law terms: (a) ion convection component in *Z* direction; (b) *z* component of the electric field in electron frame; (c) Hall term component in *Z* direction; (d) $\mathbf{E} \cdot \mathbf{J}$ dissipation; (e) electron pressure term in *Z*; and (f) agyrotropy parameter.

Additionally, Figure 3f shows the $\sqrt{Q}$ parameter introduced by *Swisdak* [2016] representing a measure of gyrotropy of the electron pressure tensor. It is defined as following

$$Q = 1 - \frac{4I_2}{\left(I_1 - P_{\parallel}\right)\left(I_1 + 3P_{\parallel}\right)}, \tag{3}$$

where $I_1 = P_{xx} + P_{yy} + P_{zz}$, $I_2 = P_{xx}P_{yy} + P_{xx}P_{zz} + P_{yy}P_{zz} - \left(P_{xy}P_{yx} + P_{xz}P_{zx} + P_{yz}P_{zy}\right)$, and $P_{\parallel} = \hat{\mathbf{b}} \cdot \mathbf{P} \cdot \hat{\mathbf{b}}$. Note that linear changes are assumed over the spacecraft tetrahedron in the electron pressure calculation; thus, shorter than spacecraft separation length scales could be underestimated [*Paschmann and Schwartz*, 2000]. For gyrotropic tensors $Q = 0$, while maximal agyrotropy is reached at $Q = 1$. The variations due to electron pressure tensor, $(\nabla \cdot \mathbf{P}_e/\mathrm{ne})_z$ (Figure 3e) are also elevated when the electric field in the electron frame (Figure 3b) is high. Similar behavior is observed at the magnetopause [*Norgren et al.*, 2016, this issue]. Finally, according to PIC simulations [*Swisdak*, 2016], the parameter $\sqrt{Q}$ reaching values about 0.05 indicates significant agyrotropy, which occurs near the separatrices or reconnection X lines. This is most pronounced at about 00:26:09.5 UT for MMS 1 (black peak in Figure 3f), note, however, that $\sqrt{Q}$ is enhanced within the whole interaction region.

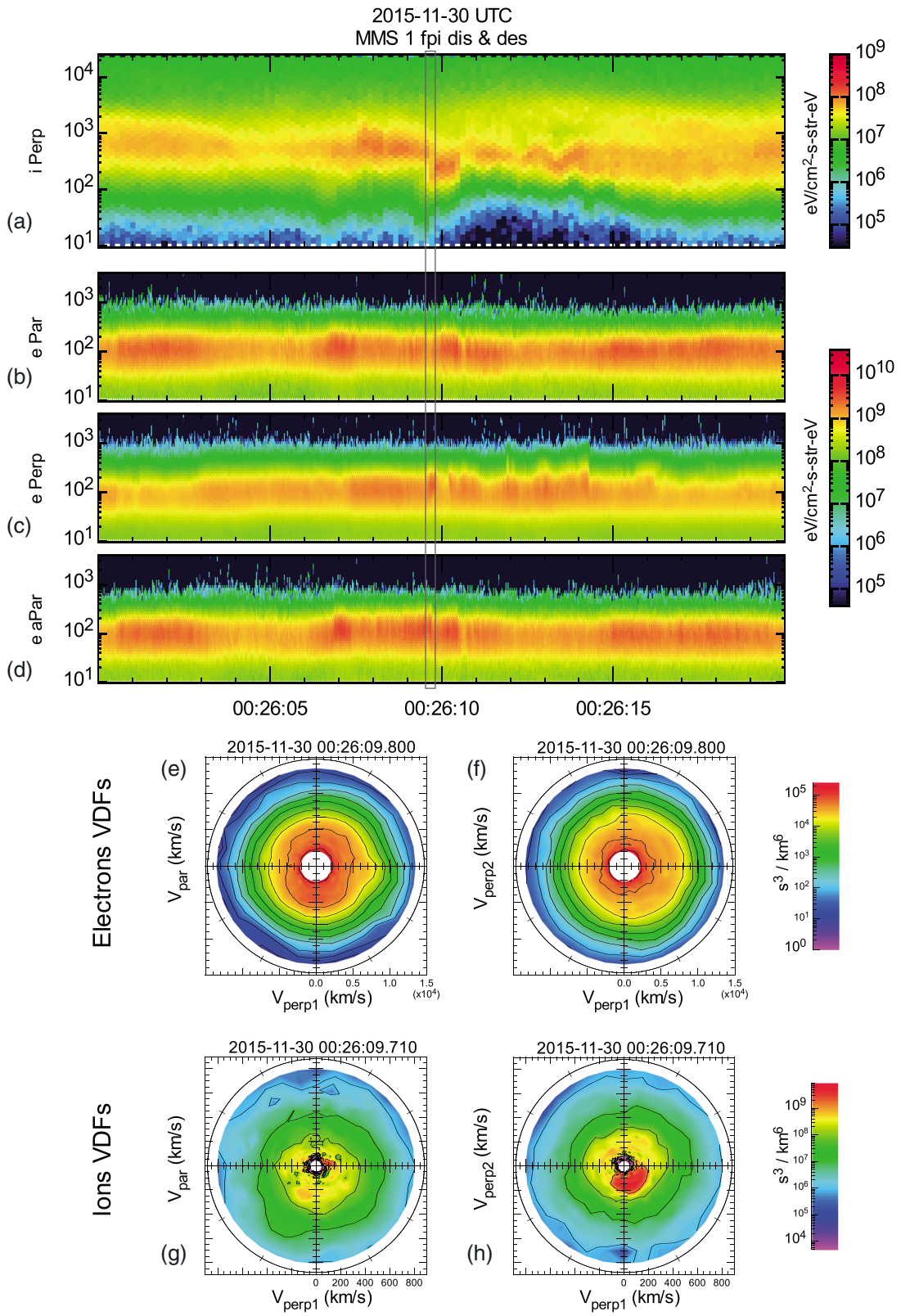

Figure 4. Particle energy spectrograms: (a) ion distribution perpendicular to the local magnetic field; (b–d) electron distribution respectively parallel, perpendicular, and antiparallel to the magnetic field. Velocity distribution functions (VDFs) cuts for electrons in directions: (e) $\mathbf{V}_{\perp_1}$ versus $\mathbf{V}_{\parallel}$ and (f) $\mathbf{V}_{\perp_1}$ versus $\mathbf{V}_{\perp_2}$; (g and h) the same VDFs cuts for ions.

6. Particle Distributions

Figure 4 represents the plasma observations by FPI ion and electron instrument on MMS 1. The top four horizontal panels are the time series energy spectrograms of the ions and electrons. Ion distribution perpendicular to the local magnetic field is shown in Figure 4a. The electrons three distributions, parallel, perpendicular, and antiparallel, to the magnetic field are presented in Figures 4b–4d, respectively. From the ion energy spectrogram (Figure 4a), it is evident that at 00:26:00 UT the ion population has an energy centered at ~750 eV. After that the flux of ions shows some variations, however, the center of energy remains the same. The first clear change occurs at ~ 00:26:07.5 UT around the time that total magnetic field reaches its minimum value, where the flux of ions is also increased. Then at ~ 00:26:09.6 UT, a distinct colder population with energies centered at ~150 eV emerges, while a lower flux population is also centered at ~400 eV. The colder magnetosheath ions are observed until ~ 00:26:10.5 UT where a higher energy population, narrowly distributed around ~500 eV, appears. The latter is the dominant population until 00:26:14.2 UT, when ions are separated in two distinct populations, one centered at ~300 eV and the other at 1 KeV. This trend continues until the end of the period at 00:26:20 UT, where the ions have one population with ~700–800 eV energy.

The energy spectrogram of the electrons shows that at the start of the period, they are mainly bistreaming (Figures 4b and 4d), which continues until ~00:26:03.4 UT when the distribution becomes rather isotropic. At ~00:26:07.1 UT, the distribution turns to bistreaming for a short period (about ~0.5 s) before the minima of the total magnetic field. The population is again isotropic until ~00:26:09.6 UT when the magnetic field $B_z = 0$. At this time, the population is predominantly antifield aligned, resulting in the velocity of electrons reaching ~600 km/s purely in that direction. This narrow region quickly passes by MMS 1, and only 0.2 s later, the electrons are observed to be moving mainly perpendicular to the magnetic field (Figure 4c) with speed of ~550 km/s, which lasted ~0.1 s. In this short interval the center of energy for the electrons quickly rise from ~100 eV to ~150 eV and then back to ~100 eV. This time interval, which is marked by the rectangle in Figure 4, is when the values of $\sqrt{Q}$ reach their maximum, representing a nongyrotropy in electron distribution. In addition to that, this signature is also accompanied with appearance of colder ion population as mentioned above (Figure 4a) and therefore is of particular interest. After this time, the perpendicular electrons (Figure 4c) show variations at 00:26:10.6, 11.9, 12.9, 14.1, and 16.1 UT, while the parallel and antiparallel stay relatively equal (Figures 4b and 4d). However, between 00:26:09.6 and 00:26:09.8 UT, it is the only time interval that the maximum velocity (Figure 1i) and a clear increase in the flux of electrons are observed (Figures 4b and 4c).

Figures 4e–4h show the velocity distribution function (VDF) of particles for a snapshot at 00:26:09.710 and 00:26:09.800 UT. The upper and bottom pair of panels are cuts of VDFs for electrons (Figures 4e and 4f) and ions (Figures 4g and 4h) in $\mathbf{V}_{\parallel}-\mathbf{V}_{\perp_1}$ and $\mathbf{V}_{\perp_1}-\mathbf{V}_{\perp_2}$ diagrams, where $\mathbf{V}_{\parallel}$ represents the velocity along the magnetic field orientation, $\mathbf{V}_{\perp_1}$ and $\mathbf{V}_{\perp_2}$, respectively, along ($\mathbf{E}\times\mathbf{B}$) and $\mathbf{B}\times(\mathbf{E}\times\mathbf{B})$ directions. The $\mathbf{V}_{\parallel}-\mathbf{V}_{\perp_1}$ plot for the electrons (Figure 4e) shows that while the lowest energy population are approximately isotropic, there is also a population which were purely moving in positive ($\mathbf{E}\times\mathbf{B}$) direction. The former population as also mentioned above is ~100 eV and the later ~150 eV. The simultaneous observations of ions, however, show that the main population (~400 eV) is antifield aligned, while there is no clear ($\mathbf{E}\times\mathbf{B}$) drifted population.

In the $\mathbf{V}_{\perp_1}-\mathbf{V}_{\perp_2}$ plot for the electrons (Figure 4f) , the population with lowest energy (< 100 eV) is gyrotropic, but the higher energy (~150 eV) population shows a clear nongyrotropy with the electrons being shifted in positive ($\mathbf{E}\times\mathbf{B}$) direction. In a ($\mathbf{E}\times\mathbf{B}$) drifted distribution in plasma, it is expected that the lower energy particles are more effected due to the relative velocity drift. However, for this case, the fact that the lower energy population is drifted less than the higher energy population, it may suggest that the latter is a distinct population. The simultaneous VDF for ions (Figures 4g and 4h) shows that the highest flux ions are predominantly moving in negative direction of $\mathbf{B}\times(\mathbf{E}\times\mathbf{B})$ directions (Figure 4h) . This population is the same cold ions centered at ~150 eV (Figure 4a), which emerged at the time of the rotation of B_z component in the magnetic field (Figure 1d). Also the lower flux ions, with energy centered at ~400 eV, are approximately gyrotropic at this time (Figure 4a).

7. Discussion and Summary

The appearance of the two distinct cold and hot populations of ions leading to a non-Maxwellian distribution suggests that these observations have taken place where ions were demagnetized [e.g., *Dai et al.*, 2015; *Zhou et al.*, 2009]. This idea is supported by the nongyrotropic shape of the ion distributions in VDF plots (Figures 4g and 4h), where an asymmetric reconnection [e.g., *Lee et al.*, 2014] can lead to mixing up distinct sources of

plasma with different energies. The separation of two populations in $\mathbf{V}_{\perp_1} - \mathbf{V}_{\perp_2}$ plane along (Figure 4h) is also consistent with previous observations of ion diffusion region by *Dai et al.* [2015] using Time History of Events and Macroscale Interactions during Substorms spacecraft.

At electron scale, the narrow region with excessive antifield-aligned electron jet, followed by a jet along ($\mathbf{E}\times\mathbf{B}$) direction in the interval where **E** field reached its maximum, suggests a possible passage of the spacecraft near the X line. Similar signatures of diffused ions followed by electron outflow with electrons frozen-in on the reconnected field line have been observed in the separatrix region in simulation of asymmetric reconnection at the magnetopause [*Khotyaintsev et al.*, 2016; *Shay et al.*, 2016, this issue]. There is also an increase in the agyrotropy parameter *Q* for the electrons, which is expected to be seen around the electron diffusion region; however, the observations are not accompanied with a crescent shaped distribution of electrons in $\mathbf{V}_{\perp_1} - \mathbf{V}_{\perp_2}$ plane [e.g., *Hesse et al.*, 1999, 2011]. Note that this crescent shape is clearer for magnetopause reconnection where the two sources of plasma have clear energy differences, while in the magnetosheath, similarly to the magnetotail [*Henderson et al.*, 2006], it may not be the case. Overall, the particle data here suggest that most of the observations are near the X line inside ion diffusion region. The spacecraft does not clearly enter the electron diffusion region; however, the nondiagonal elements of electron pressure tensor increase significantly as MMS 1 probably crossed the separatrix region. This is consistent with simulations on the spatial dimensions of the electron diffusion region [e.g., *Nakamura et al.*, 2016; *Swisdak*, 2016].

In summary, the main motivation for this study is to show that coherent structures such as flux ropes, current sheets, and reconnection associated multiscale structures can be observed over proton and electron scales in the turbulent magnetosheath by MMS spacecraft. The analyzed time interval comprised a flux rope with slightly rotating magnetic field with compressions, discontinuities, current sheets, and electron and ion scale (~0.5–30 km) structures developing at its border. In this region of interest, the four MMS spacecraft observed (1) strong electron scale currents; (2) significant *z* components of the electric field in the electron frame $(\mathbf{E}+\mathbf{V}_e\times\mathbf{B})_z$ and the Hall term $(\mathbf{J}\times\mathbf{B}/\mathrm{ne})_z$; (3) signature of demagnetized ions and ion Alfvén outflow; (4) fast electron jets; (5) electron heating; (6) $\mathbf{E}\cdot\mathbf{J}$ up to ~70 nW/m^3 at narrow peaks indicating that the electromagnetic energy is converted and dissipated; and (7) electron pressure agyrotropy. These features suggest that MMS observes MR site within electron scale current sheets in the turbulent magnetosheath plasma.

This study, complementing and further developing the ideas about turbulence-generated structures by observations in the magnetosheath [*Retinò et al.*, 2007; *Chasapis et al.*, 2015; *Vörös et al.*, 2016] and in the solar wind [*Greco et al.*, 2016] and by simulations [*Karimabadi et al.*, 2013], suggests that electron scale structures and reconnecting current sheets may occur not only at the large-scale boundaries, such as the magnetopause or magnetotail current sheet, but also in turbulent collisionless plasmas. We believe that these findings might encourage more thorough investigations of turbulence-generated structures by using the high-resolution measurements of MMS.

Acknowledgments
E.Y. and Z.V. research leading to these results has received funding from the European Community's Seventh Framework Programme ([7/2007–2013] under grant agreement 313038/STORM. Z.V. was supported by the Austrian Fond zur Förderungur der wissenschaftlichen Forschung (project P24740-N27). IRAP contribution and the French involvement to (SCM) on MMS are supported by CNES and CNRS. Y.K. and D.B.G. were supported by the Swedish National Space Board, grants 139/12 and 175/15. Parts of the particle plots presented in this paper are generated using the QSAS software.

References

Aunai, N., M. Hesse, and M. Kuznetsova (2013), Electron nongyrotropy in the context of collisionless magnetic reconnection, *Phys. Plasmas*, *20*, 092903.

Burch, J. L., T. E. Moore, R. B. Torbert, and B. L. Giles (2015), Magnetospheric multiscale overview and science objectives, *Space Sci. Rev.*, *199*, 5–21, doi:10.1007/s11214-015-0164-9.

Burch, J. L., et al. (2016), Electron-scale measurements of magnetic reconnection in space, *Science*, doi:10.1126/science.aaf2939, in press.

Chasapis, A., A. Retinó, F. Sahraoui, A. Vaivads, Y. V. Khotyaintsev, D. Sundkvist, A. Greco, L. Sorriso-Valvo, and P. Canu (2015), Thin current sheets and associated electron heating in turbulent space plasma, *Astrophys. J. Lett.*, *804*, L1.

Dai, L., C. Wang, V. Angelopoulos, and K.-H. Glassmeier (2015), In situ evidence of breaking the ion frozen-in condition via the non-gyrotropic pressure effect in magnetic reconnection, *Ann. Geophys.*, *33*, 1147–1153.

Dunlop, M. W., A. Balogh, K.-H. Glassmeier, and P. Robert (2002), Four-point Cluster application of magnetic field analysis tools: The Curlometer, *J. Geophys. Res.*, *107*(A11), 1384, doi:10.1029/2001JA005088.

Ergun, R. E., et al. (2016), The axial double probe and fields signal processing for the MMS mission, *Space Sci. Rev.*, *199*, 167–188, doi:10.1007/s11214-014-0115-x.

Fischer, D., et al. (2016), Optimized merging of search coil and fluxgate Data for MMS, *Geosci. Instrum. Method. Data Syst. Discuss*, doi:10.5194/gi-2016-11.

Greco, A., P. Chuychai, W. H. Matthaeus, S. Servidio, and P. Dmitruk (2008), Intermittent MHD structures and classical discontinuities, *Geophys. Res. Lett.*, *35*, L19111, doi:10.1029/2008GL035454.

Greco, A., S. Perri, S. Servidio, E. Yordanova, and P. Veltri (2016), The complex structure of magnetic field discontinuities in the turbulent solar wind, *Astrophys. J. Lett.*, *823*, L39, doi:10.3847/2041-8205/823/2/L39.

Graham, D. B., et al. (2016), Electron currents and heating in the ion diffusion region of asymmetric reconnection, *Geophys. Res. Lett.*, *43*, doi:10.1002/2016GL068613, in press.

Henderson, P. D., C. J. Owen, A. D. Lahiff, I. V. Alexeev, A. N. Fazakerley, E. Lucek, and H. Réme (2006), Cluster PEACE observations of electron pressure tensor divergence in the magnetotail, *Geophys. Res. Lett.*, *33*, L22106, doi:10.1029/2006GL027868.

Hesse, M., K. Schindler, J. Birn, and M. Kuznetsova (1999), The diffusion region in collisionless magnetic reconnection, *Phys. Plasmas*, *6*, 1781–1795.

Hesse, M., T. Neukirch, K. Schindler, M. Kuznetsova, and S. Zenitani (2011), The diffusion region in collisionless magnetic reconnection, *Space Sci. Rev.*, *160*, 3–23.

Karimabadi, H., et al. (2013), Coherent structures, intermittent turbulence, and dissipation in high-temperature plasmas, *Phys. Plasmas*, *20*, 012303.

Karimabadi, H., et al. (2014), The link between shocks, turbulence, and magnetic reconnection in collisionless plasmas, *Phys. Plasmas*, *21*, 062308.

Khotyaintsev, Y. V., A. Vaivads, A. Retinò, M. André, C. J. Owen, and H. Nilsson (2006), Formation of inner structure of a reconnection separatrix region, *Phys. Rev. Lett.*, *97*, 205003.

Khotyaintsev, Y. V., et al. (2016), Electron jet of asymmetric reconnection, *Geophys. Res. Lett.*, *43*, doi:10.1002/2016GL069064, in press.

Lavraud, B., et al. (2016), Currents and associated electron scattering and bouncing near the diffusion region at Earth's magnetopause, *Geophys. Res. Lett.*, *43*, 3042–3050, doi:10.1002/2016GL068359.

Lapenta, G., S. Markidis, M. V. Goldman, and D. L. Newman (2015), Secondary reconnection sites in reconnection-generated flux ropes and reconnection fronts, *Nat. Phys.*, *11*, 690–695.

Le Contel, O., et al. (2014), The search-coil magnetometer for MMS, *Space Sci. Rev.*, *199*, 257–282, doi:10.1007/s11214-014-0096-9.

Lee, S. H., et al. (2014), Plasma and energetic particle behaviors during asymmetric magnetic reconnection at the magnetopause, *J. Geophys. Res. Space Physics*, *119*, 1658–1672, doi:10.1002/2013JA019168.

Lindqvist, P.-A., et al. (2016), The spin-plane double probe electric field instrument for MMS, *Space Sci. Rev.*, *199*, 137–165, doi:10.1007/s11214-014-0116-9.

Matthaeus, W. H., M. Wan, S. Servidio, A. Greco, K. T. Osman, S. Oughton, and P. Dmitruk (2015), Intermittency, nonlinear dynamics and dissipation in the solar wind and astrophysical plasmas, *Philos. Trans. R. Soc. A*, *373*, 20140154.

Nakamura, T., R. Nakamura, and H. Hasegawa (2016), Spatial dimensions of the electron diffusion region in anti-parallel magnetic reconnection, *Ann. Geophys.*, *34*, 357–367.

Norgren, C., et al. (2016), Finite gyroradius effects in the electron outflow of asymmetric magnetic reconnection, *Geophys. Res. Lett.*, *43*, doi:10.1002/2016GL069205.

Osman, K. T., W. H. Matthaeus, M. Wan, and A. F. Rappazzo (2012), Intermittency and local heating in the solar wind, *Phys. Rev. Lett.*, *108*, 261102.

Osman, K. T., W. H. Matthaeus, J. T. Gosling, A. Greco, S. Servidio, B. Hnat, S. C. Chapman, and T. D. Phan (2014), Magnetic reconnection and intermittent turbulence in the solar wind, *Phys. Rev. Lett.*, *112*, 215002.

Paschmann, G., and S. J. Schwartz (2000), *ISSI Book on Analysis Methods for Multi-Spacecraft Data, ESA Spec. Publ.*, vol. 449, Int. Space Sci. Inst., Bern, Switz.

Pollock, C., et al. (2016), Fast plasma investigation for magnetospheric multiscale, *Space Sci. Rev.*, *199*, 331–406, doi:10.1007/s11214-016-0245-4.

Retinò, A., D. Sundkvist, A. Vaivads, F. Mozer, M. André, and C. J. Owen (2007), In situ evidence of magnetic reconnection in turbulent plasma, *Nat. Phys.*, *3*, 236–238.

Russell, C. T., et al. (2014), The magnetospheric multiscale magnetometers, *Space Sci. Rev.*, *199*, 189–256, doi:10.1007/s11214-014-0057-3.

Scudder, J. D., H. Karimabadi, W. Daughton, and V. Roytershteyn (2015), Frozen flux violation, electron demagnetization and magnetic reconnection, *Phys. Plasmas*, *22*, 101204.

Servidio, S., W. H. Matthaeus, M. A. Shay, P. A. Cassak, and P. Dmitruk (2009), Magnetic reconnection and two-dimensional magnetohydrodynamic turbulence, *Phys. Rev. Lett.*, *102*, 115003.

Servidio, S., F. Valentini, F. Califano, and P. Veltri (2012), Local kinetic effects in two-dimensional plasma turbulence, *Phys. Rev. Lett.*, *108*, 045001.

Shay, M. A., T. D. Phan, C. C. Haggerty, M. Fujimoto, J. F. Drake, K. Malakit, P. A. Cassak, and M. Swisdak (2016), Kinetic signatures of the region surrounding the X-line in asymmetric (magnetopause) reconnection, *Geophys. Res. Lett.*, *43*, 4145–4154, doi:10.1002/2016GL069034.

Swisdak, M. (2016), Quantifying gyrotropy in magnetic reconnection, *Geophys. Res. Lett.*, *43*, 43–49, doi:10.1002/2015GL066980.

Torbert, R. B., et al. (2014), The FIELDS instrument suite on MMS: Scientific objectives, measurements, and data products, *Space Sci. Rev.*, *199*, 105–135, doi:10.1007/s11214-014-0109-8.

Vörös, Z., E. Yordanova, M. M. Echim, G. Consolini, and Y. Narita (2016), Turbulence-generated proton-scale structures in the terrestrial magnetosheath, *Astrophys. J. Lett.*, *819*, L15.

Wan, M., W. H. Matthaeus, V. Roytershteyn, H. Karimabadi, T. Parashar, P. Wu, and M. Shay (2015), Intermittent dissipation and heating in 3D kinetic plasma turbulence, *Phys. Rev. Lett.*, *114*, 175002.

Zaqarashvili, T., Z. Vörös, Y. Narita, and R. Bruno (2014), Twisted magnetic flux tubes in the solar wind, *Astrophys. J. Lett.*, *783*, L19.

Zenitani, S., M. Hesse, A. Klimas, and M. Kuznetsova (2011), New measure of the dissipation region in collisionless magnetic reconnection, *Phys. Rev. Lett.*, *106*, 195003.

Zhou, X.-Z., V. Angelopoulos, A. Runov, M. I. Sitnov, Q.-G. Zong, and Z. Y. Pu (2009), Ion distributions near the reconnection sites: Comparison between simulations and THEMIS observations, *J. Geophys. Res.*, *114*, A12211, doi:10.1029/2009JA014614.